PAPER • OPEN ACCESS

Crystallinity characterization of white matter in the human brain

New Journal of Physics
The open access journal at the forefront of physics

Deutsche Physikalische Gesellschaft DPG
IOP Institute of Physics

Published in partnership with: Deutsche Physikalische Gesellschaft and the Institute of Physics

OPEN ACCESS

RECEIVED
26 March 2021

REVISED
14 June 2021

ACCEPTED FOR PUBLICATION
8 July 2021

PUBLISHED
30 July 2021

PAPER

Crystallinity characterization of white matter in the human brain

Erin G Teich[1], Matthew Cieslak[2], Barry Giesbrecht[3], Jean M Vettel[4], Scott T Grafton[3], Theodore D Satterthwaite[2] and Danielle S Bassett[1,2,5,6,7,8,*]

[1] Department of Bioengineering, School of Engineering & Applied Science, University of Pennsylvania, Philadelphia, PA 19104, United States of America
[2] Department of Psychiatry, Perelman School of Medicine, University of Pennsylvania, Philadelphia, PA 19104, United States of America
[3] Department of Psychological & Brain Sciences, University of California, Santa Barbara, CA 93117, United States of America
[4] Army Research Laboratory, Aberdeen Proving Ground, MD 21005, United States of America
[5] Department of Physics and Astronomy, College of Arts & Sciences, University of Pennsylvania, Philadelphia, PA 19104, United States of America
[6] Department of Electrical and Systems Engineering, School of Engineering & Applied Science, University of Pennsylvania, Philadelphia, PA 19104, United States of America
[7] Department of Neurology, Perelman School of Medicine, University of Pennsylvania, Philadelphia, PA 19104, United States of America
[8] Santa Fe Institute, Santa Fe, NM 87501, United States of America
[*] Author to whom any correspondence should be addressed.

E-mail: dsb@seas.upenn.edu

Keywords: diffusion MRI, white matter, crystallinity, structural characterization

Supplementary material for this article is available online

Abstract

Human brain tissue is a heterogeneous material, consisting of soft outer grey matter tethered internally by stiffer cords of white matter. These white matter tracts conduct electrical impulses between grey matter regions, thereby underpinning neuronal communication. Understanding the material properties of white matter is thus crucial for understanding brain function generally. Efforts to assess white matter microstructure are currently hampered by the inherent limitations of reconstruction by diffusion imaging. Techniques typically represent white matter structures with single scalars that are often difficult to interpret. Here, we address these issues by introducing tools from materials physics for the characterization of white matter microstructure. We investigate structure on a mesoscopic scale by analyzing its homogeneity and determining which regions of the brain are structurally homogeneous, or 'crystalline' in the context of materials physics. We find that crystallinity provides novel information and varies across the brain along interpretable lines of anatomical difference, with highest homogeneity in regions adjacent to the corpus callosum, a large interhemispheric tract. Furthermore, crystallinity is markedly reliable across iterative measurement, yet also varies between individual human volunteers, making it potentially useful for examining individual differences in white matter along several dimensions including sex and age. We also parcellate white matter into 'crystal grains', or contiguous sets of voxels of high structural similarity, and find overlap with a common atlas of distinct white matter areas. Finally, we characterize the shapes of individual diffusion signatures through another tool from materials physics—bond-orientational order parameters—to locate fiber crossings and fascicles. Our results provide new means of assessing white matter microstructure on multiple length scales, and open multiple avenues of future inquiry involving soft matter physics and neuroscience.

1. Introduction

Brain tissue is a heterogeneous material whose constituent components, grey matter and white matter, have distinct physical properties and distinct functions. Grey matter, distributed near and on the cortical surface, performs a majority of the cellular computation necessary for perception, attention, memory, thought, language, and general human functioning [1]. Communication between cortical areas occurs in part by the conduction of electrical impulses along stiffer cords of underlying white matter [2, 3], whose architecture is a critical constraint on information transmission in the brain. White matter microstructure thus enables normal brain function, cognition, and behavior [4, 5]. Disruption of these connections is hypothesized to contribute to a variety of pathologies that may arise in abnormal development and following injury and aging [6–10]. Reliable and thorough characterization of the material properties of white matter is accordingly a scientific challenge of enormous import. That these measurements are non-invasive is also critical for meeting ethical standards when studying white matter in humans. Accurate and detailed measurements of white matter in living human brains enables better detection of disease and contributes to the growing body of knowledge regarding the influence of development and aging on brain structure.

Diffusion MRI provides a non-invasive means of characterizing microstructure in biological tissues [11–13]. In diffusion imaging, the orientation of myelinated white matter, and proxies for its microstructural properties, are typically estimated in millimeter-scale regions (or voxels) of the brain based on observed magnetic resonance signal changes related to water diffusion. White matter orientation distribution functions (ODFs) in each voxel are constructed from three-dimensional probability densities of water diffusion via radial integration, such that the magnitude of the ODF at any point on the unit sphere is proportional to the water diffusion probability in that direction [14]. ODFs in each voxel thus constitute local structural signals that can be analyzed further, including for the tracking of large white matter fascicles [15] between cortical regions, or the monitoring of the loss of white matter integrity that often accompanies aging [16, 17] or the progression of neurodegenerative diseases such as mild cognitive impairment [18], Alzheimer's disease [8, 19], multiple sclerosis [8, 20], ALS [21], or general Wallerian degeneration [22].

Strategies for the characterization of white matter structure using diffusion imaging data, each with their own advantages and drawbacks, abound. Many techniques reduce dimensionality by representing aspects of intra-voxel structure such as anisotropy as single voxel-wise scalars [14]. These scalars, however, are often difficult to interpret or rely on oversimplified tensor models of diffusion. Other techniques measure white matter coherence on larger, inter-voxel length scales through the calculation of voxel-wise scalars such as the lattice index [23] and tensor overlap [24]. However, these metrics also rely on simple tensor models for diffusion that do not fully capture its more complicated phenomenology. A notable exception is so-called local diffusion homogeneity, which represents inter-voxel white matter coherence in a model-free manner [17]. Instead, however, this coherence metric requires substantial data for its calculation as it incorporates a large amount of information collected during diffusion imaging.

Here, we introduce tools from *materials physics* to characterize white matter coherence and other features in a manner that is intuitive, simple to compute, and model-independent. Materials science, and more specifically soft matter physics, is an ideal lens through which to examine white matter microstructure: like neuroimaging, soft matter physics is often concerned with (usually messy) local structure and its relationship to macroscale (material) function. We calculate structural homogeneity (a metric commonly used in soft matter to characterize particle ensembles) as a measure of white matter coherence in the human brain. Our approach complements prior efforts to assess coherence [25], but differs from those efforts by utilizing techniques explicitly grounded in materials physics to understand brain organization. We determine which regions of the brain are structurally homogeneous, or 'crystalline' in the context of materials science, and which are structurally heterogeneous, or 'disordered'. We find that white matter homogeneity, or crystallinity, provides information about neuronal architecture that is distinct from that provided by other structural measurements often used in the neuroimaging community such as generalized fractional anisotropy (GFA) and mean diffusivity (MD). White matter crystallinity is also reliable and reproducible across multiple imaging scans of the same subject, but variable across subjects. Thus, this novel metric may be a useful marker to distinguish individual differences in white matter microstructure. In general, crystallinity varies throughout the brain, and is highest for its most internal white matter regions, including the corona radiata, internal capsule, corpus callosum, and uncinate fasciculus. These are white matter tracts situated near the center of the brain with a variety of connective purposes [2, 26]. Several of these tracts are also particularly vulnerable to pathologies including schizophrenia, bipolar disorder, and autism spectrum disorder [27]. Additionally, we find that parcellation of white matter into 'crystal grains', or spatially contiguous sets of voxels of high structural similarity, results in a new white matter partition that has partial overlap with a commonly used white matter atlas, but incorporates the distinct local morphologies of brain tissue. Taken together, our results illustrate that

crystallinity is a fruitful new means of analyzing the structure of white matter, with multiple future promising directions.

Crystallinity inherently characterizes white matter structure on a super-voxel level; however, structural characterization on the smaller, intra-voxel scale is a complementary and active research thrust within diffusion imaging. Shape characterization of the diffusion signal is of particular interest. Previously proposed metrics such as the mode of anisotropy [28] give some indication of diffusion signal shape, but do not capture higher-order symmetries of the signal. For this purpose, tools from soft matter are also useful. We use bond-orientational order parameters, originally developed to measure symmetries of particle clusters in supercooled liquids and glasses [29], to provide a low-dimensional characterization of ODF shape. We show that these orientational order parameters are sensitive to local white matter symmetries and provide useful, rotationally-invariant information regarding where white matter tracts are especially aligned or where they cross. Our results provide further evidence that approaches grounded in materials physics are useful for the structural characterization of the human brain as a complex soft material on multiple length scales. We look forward to future interdisciplinary extensions of this work, bridging soft matter physics and neuroimaging.

2. Methods

2.1. Diffusion image analysis

We use two datasets throughout this paper that each have particular strengths relevant to our distinct goals. The first, used to illustrate our methods, is the publicly available example of a high angular resolution diffusion image (the 'Stanford HARDI' dataset) with 160 gradient directions, distributed with the Python module *dipy* [30]. We estimate fiber orientation distributions (FODs) on the Stanford HARDI data using constrained spherical deconvolution [31] and extract FOD peaks using *dipy*. An example slice of these FODs in an array of neighboring voxels is shown in figure 1(A).

We chose a second data set to showcase the performance of our methods in detecting individual differences reliably across scans. Specifically, we use an extensive set of diffusion images collected as part of the cognitive resilience and sleep history (CRASH) study [32]. In addition to a host of other measurements, the CRASH study gathered 8 diffusion MRI scans for 30 subjects, taken bi-weekly. Subjects (13 males; 17 females) ranged in age between 18 and 35 years, with a mean age of 23 years. The diffusion acquisitions used a bipolar pulse sequence to sample a Cartesian grid in q-space at 258 coordinates with a maximum b-value of 5000 s mm^{-2} with 1.8 mm isotropic voxel size. Images were preprocessed using QSIPrep [33], which included MP-PCA denoising [34] and head motion correction. Preprocessed images were reconstructed using generalized q-sampling imaging (GQI) [35]. GQI ODFs and peaks were calculated in DSI studio, and a group threshold of 0.02 was used to threshold ODF peaks. T1-weighted anatomical scans were registered to the MNI 2009 asymmetric nonlinear template using ANTs [36].

2.2. Crystallinity

We characterize diffusion signal homogeneity across neighboring voxels by computing the 'crystallinity' of each ODF. Crystallinity measures the similarity between the structural environment of each voxel (consisting of the peak vectors extracted from each ODF signal) and the environments of its neighboring voxels. Voxels of especially high crystallinity contain ODF peaks that are especially similar, on average, to ODF peaks in neighboring voxels. Voxels of especially low crystallinity contain ODF peaks that are dissimilar from ODF peaks of neighboring voxels; these voxels are 'disordered' in the language used by the soft matter physics community. To quantify crystallinity, we measure the average deviation between the ODF peak vectors of each voxel and those of its neighbors using an environment-matching module in the open-source analysis toolkit *freud* [37]. We then normalize this deviation by the overall diffusion signal strength in the appropriate voxel, creating a dimensionless parameter ($\tilde{\Delta}$) that acts as a proxy for crystallinity.

We now provide the mathematical details of this process. For all neighboring voxel pairs i and j (defined as neighbors if the voxel boundaries share faces, edges, or vertices), we measure the root-mean-squared deviation, Δ_{ij}, between their environments:

$$\Delta_{ij} = \sqrt{\langle \delta^2_{mm'} \rangle}. \tag{1}$$

This calculation is shown schematically in figure 1(B). In the above expression, $\delta_{mm'} \equiv |\boldsymbol{r}_{im} - \boldsymbol{r}_{jm'}|$ is the magnitude of the vector difference between voxel i's mth ODF peak vector $\boldsymbol{r}_{im}$ and voxel j's m'th ODF peak vector $\boldsymbol{r}_{jm'}$. The average $\langle \delta_{m,m'} \rangle$ is taken over the mapping (m, m') found that greedily minimizes Δ_{ij}. To obtain this mapping, we consider each vector in the set $\{\boldsymbol{r}_{jm'}\}$ in turn, and pair it with the closest vector in

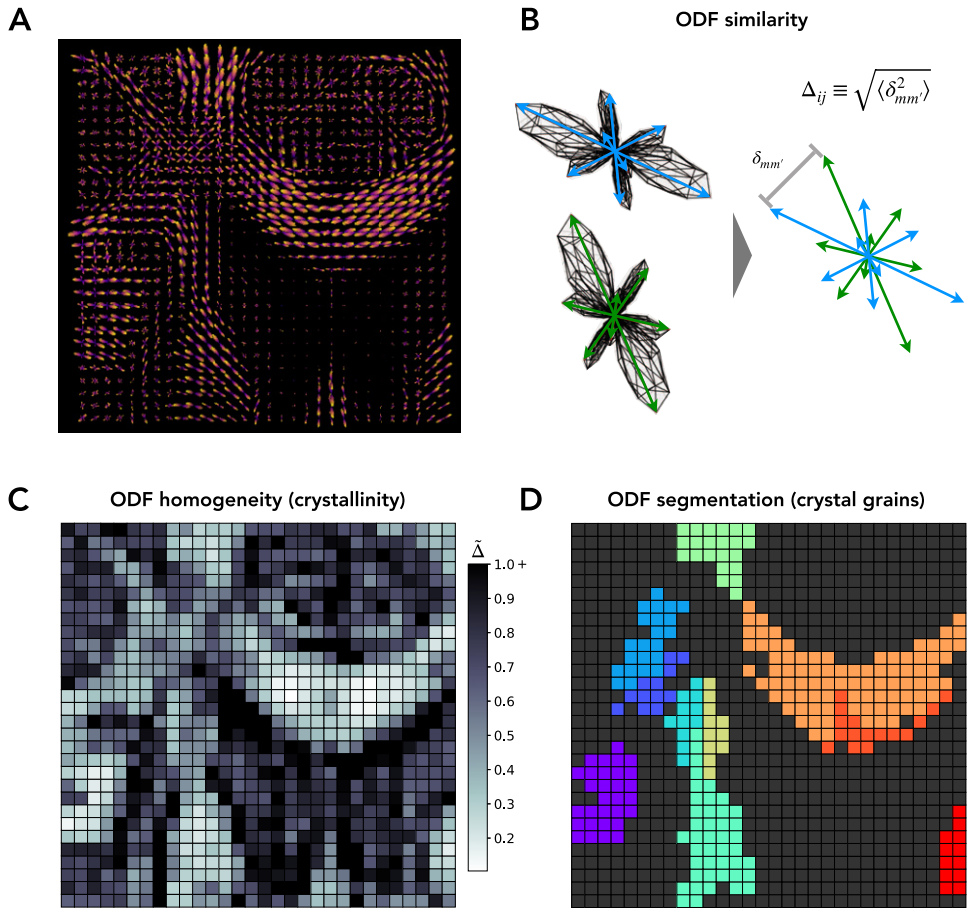

Figure 1. Crystallinity characterization methods used to analyze diffusion images of the human brain. (A) Slice of a sample diffusion image, showing the ODF signals reconstructed in each voxel. Each ODF surface is colored according to signal magnitude using a default rendering technique in the *dipy* Python package: surface points of large ODF magnitude (thus high water diffusion probability) are colored more yellow, while surface points of small ODF magnitude (thus low water diffusion probability) are colored more purple. (B) Schematic of our method for ODF similarity characterization via peak vector matching. Peak vectors are extracted from ODF distributions, and these vector sets are compared to find the best match between them, characterized by the lowest value of Δ_{ij}. (C) The identical diffusion image slice as that of panel (A), with voxels colored according to ODF homogeneity (crystallinity) according to the colorbar shown. Voxels with lower values of $\tilde{\Delta}$ are lighter (more crystalline), and voxels with higher values of $\tilde{\Delta}$ are darker (less crystalline). (D) The identical diffusion image slice as that of panel (A), with voxels colored according to segmentation by crystal grain. Voxels are colored identically if they are members of the same crystal grain. Voxels colored black are members of crystal grains of 10 or fewer voxels, or are not members of a crystal grain at all. Otherwise, color has no additional meaning.

the set $\{\boldsymbol{r}_{im}\}$ that is unpaired. If voxels i and j do not have equivalent numbers of ODF peak vectors, then we first augment the smaller set of vectors with $\mathbf{0}$ vectors until both sets are the same size before finding the (m, m') mapping. Augmentation in this manner provides a means of directly comparing peaks one-to-one without losing any peak information or relying on additional thresholding.

From the set of root-mean-squared deviations Δ_{ij} between the environment of voxel i and each of its neighbors j, we can define the normalized average deviation of voxel i's environment from those of its neighbors:

$$\tilde{\Delta}_i = \frac{\langle \Delta_{ij} \rangle}{\langle r_{im} \rangle}. \tag{2}$$

This measure is our proxy for crystallinity for each voxel. The numerator is the average Δ_{ij} between voxel i and its N_i neighbors, $\langle \Delta_{ij} \rangle \equiv \frac{1}{N_i} \sum_j \Delta_{ij}$. The denominator is the average magnitude of the M_i ODF peaks in voxel i, $\langle r_{im} \rangle = \frac{1}{M_i} \sum_m r_{im}$, excluding any augmented $\mathbf{0}$ vectors. The parameter $\tilde{\Delta}_i$ is thus normalized such that it gives the average deviation of the diffusion signal i from its neighboring signals as a fraction of that signal's average magnitude. This measure is low when crystallinity is high, and vice versa.

To gain an intuition for the spatial distribution of the measure $\tilde{\Delta}$, we show this value for each voxel in a slice through the example HARDI image described previously (figure 1(C)). Each voxel is colored according to $\tilde{\Delta}$ such that those with lower values of $\tilde{\Delta}$ (i.e. more crystalline) are lighter. Note that white matter structure can be clearly visualized by this metric. Other interesting structural features emerge as well, such

as voxels that mark 'grain boundaries' between spatially contiguous sets of voxels of high structural similarity (or 'crystal grains').

2.3. Crystal grain parcellation

We also use structural similarity between neighboring voxels to construct white matter parcellations that reflect homogeneous regions of brain tissue. We refer to these structurally similar regions as crystal grains, and formally identify them as strongly intra-connected submodules, or communities, in a network representation of each brain scan. In this representation, each voxel is a node of the network, and edges between nodes are weighted according to the structural similarity of the corresponding voxels. Edges only exist between node pairs that correspond to neighboring voxel pairs. Specifically, the edge weight W_{ij} between nodes i and j is defined as:

$$W_{ij} = \frac{1}{\frac{\Delta_{ij}}{N_{ij}} + 1}. \tag{3}$$

The parameter Δ_{ij} is the root-mean-squared deviation between the diffusion signals of voxels i and j as defined previously. We note that we set $\Delta_{ij} = \Delta_{ji}$ for computational efficiency when computing this quantity over all neighbor pairs, and this equality always holds if Δ_{ij} is a true global minimum. The parameter $N_{ij}^2 \equiv \langle \boldsymbol{r}_{im}^2 + \boldsymbol{r}_{jm'}^2 \rangle$, with the average taken over the mapping (m, m') found that greedily minimizes Δ_{ij}. As before, $\boldsymbol{r}_{im}$ is voxel i's mth ODF peak vector. The parameter N_{ij} is thus a normalization factor that represents the root-mean-squared deviation over all paired vectors if each pair of vectors was orthogonal. When diffusion signals are structurally identical, that is, $\Delta_{ij} = 0$, then edge weight is highest ($W_{ij} = 1$). As the structural similarity between diffusion signals decreases and Δ_{ij} increases, the edge weight decreases to 0.

Within this network representation, we identify crystal grains of homogeneous structure by using a Louvain-like locally greedy algorithm [38] to identify communities of nodes (voxels) that are densely intra-connected and sparsely inter-connected [39]. The algorithm maximizes the so-called modularity [40] Q of the network, which is defined as:

$$Q = \sum_{ij} \left[W_{ij} - \gamma P_{ij} \right] \delta(c_i, c_j). \tag{4}$$

The scalar W_{ij} is the edge weight between nodes i and j, P_{ij} is the expected edge weight between those nodes in a suitably-chosen null model, $\delta(c_i, c_j)$ is a Kroenecker delta that is 1 if i and j are in the same community (i.e. if community indices $c_i = c_j$) and 0 otherwise, and γ is a free scalar parameter. The parameter γ controls the resolution over which communities are detected. As γ goes to 0, $W_{ij} - \gamma P_{ij}$ becomes positive for all edge weights, and so maximizing Q consists of grouping all connected nodes into the same community. In contrast, higher γ provides a threshold for which edge weights will contribute positively to Q, and effectively filters communities such that they consist only of the most strongly-connected nodes.

Many different null models are employed in the literature, each specific to the data and scientific question of interest. Here, we use a geographical null model [41, 42] previously utilized to detect communities in spatially-embedded and locally-connected networks. In this model, $P_{ij} = \rho A_{ij}$, where $\rho = \langle W_{ij} \rangle$ is the mean edge weight of the network and A_{ij} is 1 if nodes i and j have an edge between them and 0 otherwise. This null model effectively encodes the physical constraints experienced by the system: namely, that each voxel is only structurally compared with its spatially adjacent neighbors.

Maximization of Q at a specific value of γ is accomplished by varying c, the partition of network nodes into communities. In our context, this process results in the clustering of voxels into spatially contiguous communities whose members are more structurally similar to each other than the scaled average similarity given by $\gamma \langle W_{ij} \rangle$. Each community is a 'crystal grain'. In practice, the algorithm that maximizes Q is not guaranteed to find the global optimum [43], so we perform modularity maximization 5 times and use the clustering that results in the maximum Q value.

We provide intuition for how crystal grains subdivide white matter by showing a crystal grain partition c, obtained from modularity maximization at $\gamma = 1.1$, in a slice through the example HARDI image described previously (figure 1(D)). Voxels are colored identically if they are members of the same crystal grain. Grains reflect regions of white matter with similar structure; note the large grains that correspond to the corpus callosum, superior longitudinal fasciculus, and surrounding regions. Here we have used a single γ resolution parameter for illustrative purposes. It remains of interest, however, to study the structure, morphology, and location of crystal grains over a range of resolutions. Accordingly, in a later section of this paper devoted to generating white matter parcellations according to crystal grain, we vary γ and show that across a range of γ values we obtain parcellations that are statistically similar to a white matter atlas currently used in the literature.

The white matter parcellation against which we choose to compare our results is the commonly referenced Johns Hopkins University (JHU) atlas [44], which was generated by hand segmentation of an average diffusion MRI tensor map over 81 adults. We quantify the similarity between our parcellations (over a range of γ values) and the JHU atlas via two distinct measures of partition overlap: the adjusted RAND (adj. RAND) index [45] and the adjusted mutual information (adj. MI) [46] between the partitions. The RAND index between two partitions measures the fraction of pairs of elements in the system whose mutual classification is in agreement across both partitions; that is, the fraction of element pairs determined in both partitions either to belong to the same cluster or to belong to different clusters. The mutual information between two partitions gives the difference between the entropy of one partition and the conditional entropy of that same partition given the other; in other words, it measures the reduction in the information needed to encode one partition given that the other is known. Adjusted versions of both measures correct for chance according to a permutation model, and normalize such that both measures are bounded above by 1, corresponding to exact agreement between partitions. Calculation of both metrics is performed using the Python module *scikit-learn* [47].

2.4. Other diffusion metrics

We demonstrate the novelty of the information communicated by our crystallinity parameter $\tilde{\Delta}$ by comparing it to four common per-voxel structural metrics. Here, we briefly describe these parameters: GFA, fractional anisotropy determined from diffusion tensor fitting (DTI-FA), the isotropic diffusion component (ISO), and MD. GFA, the standard deviation of the ODF signal over its entire surface (normalized by the root-mean-square of the signal over its surface), is a unitless parameter that indicates the degree of anisotropy in the diffusion signal [48]. DTI-FA is very similar in spirit to GFA; it is the standard deviation of the eigenvalues of the diffusion tensor, normalized by their root-mean-square [49]. ISO, the isotropic part of the ODF signal, is simply the minimum value of the ODF in each voxel [35]. MD, the mean of the eigenvalues of the diffusion tensor in each voxel, characterizes the overall strength of the diffusion signal [49].

2.5. Test-retest reliability and variability

We confirm that our crystallinity metric $\tilde{\Delta}$ is well-behaved as a structural marker by calculating statistical proxies for reliability, reproducibility, and across-individual variability of $\tilde{\Delta}$ and other diffusion metrics.

Reliability. To measure reliability, we use two variants of the intra-class correlation coefficient (*ICC*). In general, the ICC reports variance of interest (in our case, variance of the metric across subjects) as a fraction of total variance. When this fraction is high, the metric reliably differentiates individuals from each other, because variance across individuals is the majority contributor to the total variance. We consider both per-voxel and per-image measures of *ICC*; the former is useful to indicate the spatial variance of reliability throughout the brain, while the latter condenses the reliability of the metric over an entire scan into one easily-interpretable scalar.

The per-voxel *ICC* variant that we calculate, usually denoted by $ICC(3,1)$ [50], uses a model with fixed imaging session effects and random subject effects to describe the value of each metric in each voxel; in other words, total variance does not include effects due purely to across-scan variability. The quantity $ICC(3,1)$ can thus be thought of as a measure of consistency across scans, rather than absolute agreement across scans [51]. Note that throughout the rest of the paper we will use the terms '(imaging) session' and 'scan' interchangeably.

We calculate $ICC(3,1)$ for each voxel as follows:

$$ICC(3,1) = \frac{\mathrm{MS_{BS}} - \mathrm{MS_E}}{\mathrm{MS_{BS}} + (k-1)\mathrm{MS_E}}. \tag{5}$$

Here MS refers to the mean sum of squares, which we measure using a two-way analysis of variance (ANOVA). Specifically, $\mathrm{MS_{BS}}$ is the between-subject mean sum of squares, and $\mathrm{MS_E}$ is the residual mean sum of squares, after accounting for between-subject and between-scan sums of squares. The quantity $k = 8$ is the number of scans per subject.

We use the image intra-class correlation coefficient (*I2C2*) [52] as a second, per-image measure of reliability. The *I2C2* is a generalization of the *ICC*:

$$I2C2 = 1 - \frac{\mathrm{Tr}(K_U)}{\mathrm{Tr}(K_W)}. \tag{6}$$

Here K_W is the covariance matrix of the image vector W, where each entry of W is the value of the metric in each voxel, concatenated over all subjects and all sessions. The matrix K_U is the covariance matrix of the measurement error vector U over voxels, concatenated over all subjects and all sessions. We calculate *I2C2* for all metrics using the R package that accompanies reference [52].

Reproducibility. To measure reproducibility, or agreement of each metric across multiple scans of the same subject, we calculate the within-subject coefficient of variation, $\mathrm{CV_{WS}}$, for each voxel:

$$\mathrm{CV_{WS}} = \frac{1}{\mu}\sqrt{\frac{1}{n}\sum_i \frac{1}{k-1}\sum_j \left(X_{ij} - \bar{X}_i\right)^2}. \tag{7}$$

Here, n is the number of subjects, k is the number of scans per subject, X_{ij} is the value of the metric measured in subject i and scan j, $\bar{X}_i \equiv \sum_j X_{ij}/k$ is the across-scan average of the metric for subject i, and μ is the grand mean of X_{ij} over all subjects and scans. In practice, we calculate $\mathrm{CV_{WS}}$ using a two-way ANOVA: $\mathrm{CV_{WS}} = \frac{1}{\mu}\sqrt{\mathrm{MS_{WS}}}$, where $\mathrm{MS_{WS}}$ is the within-subject mean sum of squares. When $\mathrm{CV_{WS}}$ is low, within-subject variation is low compared to its mean, and reproducibility is high.

Individual variability. We finally measure across-individual variability by calculating the between-subject coefficient of variation, $\mathrm{CV_{BS}}$, for each voxel:

$$\mathrm{CV_{BS}} = \frac{1}{\mu}\sqrt{\frac{1}{n-1}\sum_i \left(\bar{X}_i - \mu\right)^2}. \tag{8}$$

All variables are the same as those defined for $\mathrm{CV_{WS}}$. In practice, we calculate $\mathrm{CV_{BS}}$ again via a two-way ANOVA, and use $\mathrm{CV_{BS}} = \frac{1}{\mu}\sqrt{\mathrm{MS_{BS}}/k}$, where $\mathrm{MS_{BS}}$ is the between-subject mean sum of squares.

2.6. Orientational order parameters

To describe diffusion signal shape within each voxel, we use orientational order parameters that were first proposed by Steinhardt *et al* [29] to characterize the symmetries of particle clusters in supercooled liquids and glasses. Consider that the diffusion signal can be represented as a probability density distribution on the unit sphere. This distribution, in turn, can be expressed as a linear combination of the spherical harmonics, a set of basis functions on the unit sphere:

$$f(\theta,\phi) = \sum_{l=0}^{\infty}\sum_{m=-l}^{l} q_{lm} Y_{lm}(\theta,\phi).$$

Here, Y_{lm} is the spherical harmonic associated with angular momentum number l and magnetic quantum number m, and q_{lm} is the projection of $f(\theta,\phi)$ onto Y_{lm}. Using the Fourier coefficients q_{lm}, we construct the following orientational order parameter (sometimes also called a Steinhardt order parameter in the soft matter literature) to characterize the symmetry of the distribution associated with angular momentum number l:

$$Q_l = \sqrt{\frac{4\pi}{2l+1}\sum_m |q_{lm}|^2}. \tag{9}$$

It can be shown that this parameter is rotationally invariant; that is, it does not change under any rigid rotation of $f(\theta,\phi)$. A finite collection of Q_l parameters for different values of l is thus a rotationally-invariant, dimension-reduced fingerprint for the associated $f(\theta,\phi)$ distribution. Rotational invariance is a useful property for any shape descriptor, because it means the descriptor depends only on the details of the shape geometry and not on its relative orientation with respect to an arbitrary reference frame.

3. Results

3.1. Crystallinity measures novel information

We first demonstrate that crystallinity varies across the brain in a meaningful and interpretable way, and provides new structural information that is not measured by other diffusion metrics commonly used in the neuroimaging community. We calculate crystallinity in two separate datasets, and compare it to two other diffusion metrics, GFA and MD, described in the *Methods*. We choose GFA and MD as our metrics of comparison because they measure very distinct aspects of the diffusion signal; thus, that crystallinity is distinct from each of them demonstrates its novelty.

As an initial benchmark, we first compute the crystallinity of each voxel in the example HARDI image described in the *Methods*. Figure 2(A) shows three views of the HARDI image, with each voxel represented as a sphere and colored according to $\tilde{\Delta}$, and figure 2(B) shows the corresponding histogram of $\tilde{\Delta}$. Regions of high and low crystallinity clearly emerge, and the corpus callosum, corona radiata, internal capsule, and anterior commissure appear as regions of high crystallinity. We directly compare crystallinity to common diffusion metrics by plotting joint distributions of $\tilde{\Delta}$ and MD across all voxels, and $\tilde{\Delta}$ and GFA across all

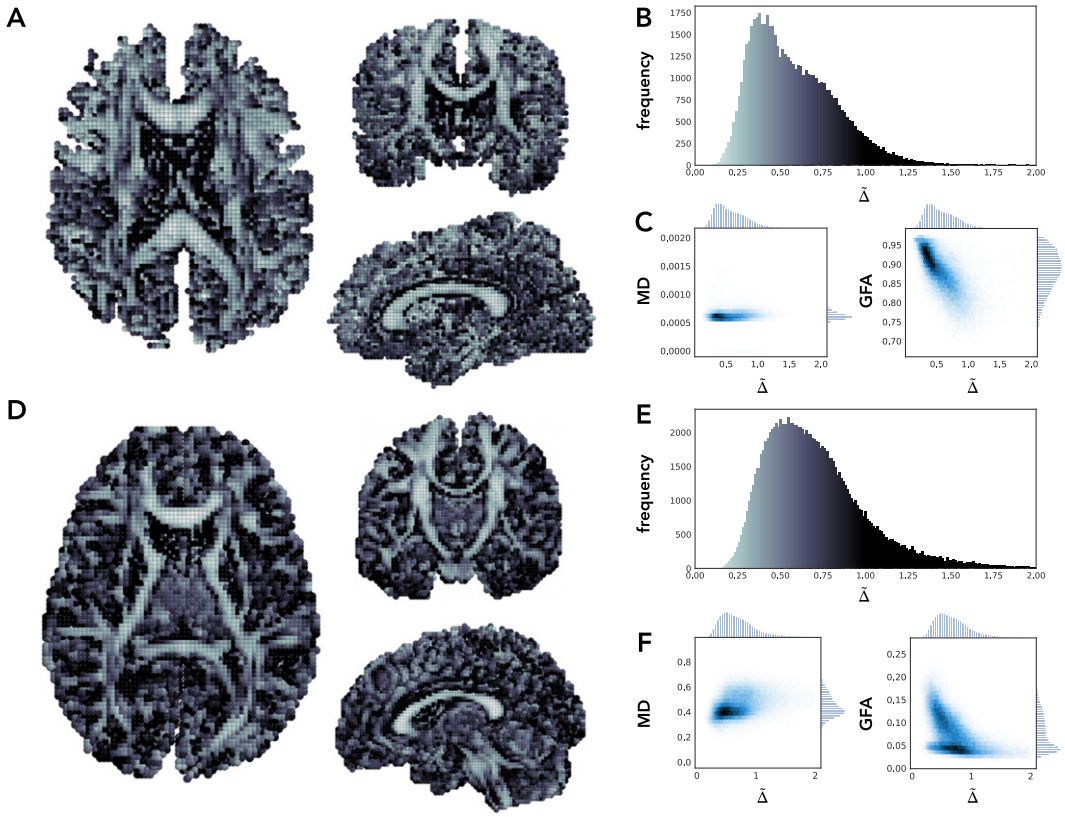

Figure 2. Crystallinity is sensitive to biological microstructure while providing novel information compared to common measures. (A) Three views of a sample diffusion image, where voxels are represented as spheres and colored according to $\tilde{\Delta}$. (B) Histogram of the $\tilde{\Delta}$ values calculated for the voxels of this sample diffusion imaging scan. Bars are colored to illustrate the coloring scheme used in panel (A). Voxels with lower values of $\tilde{\Delta}$ are lighter (more crystalline), and voxels with higher values of $\tilde{\Delta}$ are darker (less crystalline). (C) Joint histograms of $\tilde{\Delta}$ against mean diffusivity (MD; left panel) as well as generalized fractional anisotropy (GFA; right panel), accumulated over the voxels of the sample scan. (D) Three views of a session-averaged diffusion image for one subject in the CRASH study, with voxels colored according to $\tilde{\Delta}$ averaged across scans. (E) Histogram of session-averaged $\tilde{\Delta}$ values calculated for the voxels of this subject. Bars are colored to illustrate the coloring scheme used in panel (D). (F) Joint histograms of $\tilde{\Delta}$ against mean diffusivity (MD; left panel) as well as generalized fractional anisotropy (GFA; right panel), accumulated over the voxels in one imaging session of the same subject.

voxels (figure 2(C)). The joint distributions show that crystallinity is weakly correlated with MD (Pearson correlation coefficient $\rho = 0.19$), and is more correlated with GFA (Pearson correlation coefficient $\rho = -0.69$), since voxels of high GFA tend to be more crystalline, with lower values of $\tilde{\Delta}$. This correlation implies physically meaningful information about white matter microstructure on multiple length scales, since GFA measures structural information within each voxel, whereas crystallinity measures structural information on an across-voxel length scale. Specifically, the correlation implies that voxels of high GFA tend to exist within white matter fascicles, where water diffuses in the same direction throughout neighboring voxels, and they thus have homogeneous structure (and high crystallinity). In contrast, voxels with lower values of GFA have wider ranges of crystallinity, demonstrating that crystallinity provides information that is distinct from diffusion anisotropy, especially in areas that do not contain streamlined white matter.

To demonstrate that crystallinity provides novel information in real datasets, we also analyze diffusion images collected as part of the CRASH study described in the *Methods*. We take advantage of the multiple scans provided for each subject in this dataset to obtain smoother across-session averages of voxel-wise crystallinity, $\langle\tilde{\Delta}\rangle_{\text{scan}}$, which we show in figures 2(D) and (E) for one CRASH subject. This crystallinity brain map is qualitatively consistent with the one calculated for the example HARDI image (figure 2(A)): crystalline regions emerge throughout the brain, including the corpus callosum, corona radiata, internal capsule, and anterior commissure. 'Grain boundaries', or voxels of lower crystallinity on the boundary of regions of higher crystallinity, can also be seen. Note that the $\tilde{\Delta}$ distributions shown in figures 2(B) and (C) and figures 2(E) and (F) exclude outliers of extremely low crystallinity (high $\tilde{\Delta}$) for visual clarity; in fact, outlier values of $\tilde{\Delta}$ can be as large as $\tilde{\Delta} \sim 7$ in both datasets. These outliers are not localized to any particular anatomical region (supplementary figure S1 (https://stacks.iop.org/NJP/23/073047/mmedia)), and instead arise simply because of the normalization procedure we use to calculate $\tilde{\Delta}$. Values of $\tilde{\Delta}$ for each

ODF signal are normalized by $\langle r \rangle$, the average magnitude of that signal's peak vectors, to non-dimensionalize $\tilde{\Delta}$. As a consequence, signals of small strength $\langle r \rangle$ may have outlier values of $\tilde{\Delta}$ if they are neighbored by signals of higher strength. The correlation between low $\langle r \rangle$ and large outlier values of $\tilde{\Delta}$ is shown in supplementary figure S2 for all scans of all analyzed subjects in the CRASH dataset.

We again compare crystallinity to the structural metrics MD and GFA via joint distributions across voxels. Figure 2(F) shows distributions for one scan of the subject represented in figures 2(D) and (E). We find similar relationships between the metrics as those found for the HARDI example (figure 2(C)). Namely, $\tilde{\Delta}$ is less correlated with MD and more correlated with GFA, with lower values of $\tilde{\Delta}$ for voxels of higher GFA. These relationships are quantified in supplementary figure S3, which shows the distribution of Pearson correlation coefficients between $\tilde{\Delta}$ and MD (median $\rho = 0.37$, interquartile range 0.03), and the distribution of Pearson correlation coefficients between $\tilde{\Delta}$ and GFA (median $\rho = -0.58$, interquartile range 0.04), collected over all scans of all analyzed subjects. The joint distribution of $\tilde{\Delta}$ and GFA in figure 2(F) shows, even more clearly than the distribution for the HARDI example, that crystallinity and GFA are correlated at high GFA and low $\tilde{\Delta}$ (high crystallinity), reflecting white matter fascicles that contain structurally similar signatures of anisotropic water diffusion. In contrast, crystallinity and GFA are increasingly independent metrics as GFA decreases. Voxels of lower anisotropy have larger ranges of $\tilde{\Delta}$, and indeed an entire set of voxels of low GFA ~ 0.05 has the widest range of $\tilde{\Delta}$ values, between $\tilde{\Delta} = 0$ and $\tilde{\Delta} = 2$. These voxels include non-white matter regions of the brain (supplementary figure S4) that have more isotropic diffusion signals.

3.2. Test-retest reliability and variability across individuals

To confirm that our crystallinity metric $\tilde{\Delta}$ is a well-behaved structural marker whose variation is meaningful, we assess the reliability, reproducibility, and across-individual variability of $\tilde{\Delta}$ and the four common diffusion metrics described in the *Methods*, and compare these quantities. We find that crystallinity is reliable and fairly reproducible, and has higher across-individual variability than the other common diffusion metrics. Our results together indicate that crystallinity may be useful to distinguish individual differences in white matter along the dimensions of sex, genetics, and physiology.

We measure all diffusion metrics in 8 scans each of 25 subjects in the CRASH study, and calculate statistical quantities for each metric that are proxies for reliability, reproducibility, and across-individual variability, in the spirit of prior work [53–56]. Details of each statistical quantity can be found in the *Methods*. We then warp the scalar fields for each metric and each scan into a master template space via the nearest-neighbor interpolation method in ANTs [36], to facilitate voxel-wise comparison across subjects.

Reliability. We find that $\tilde{\Delta}$ is very reliable across subjects according to both $ICC(3,1)$ and $I2C2$ (figures 3(A) and (B)). The value of $I2C2$ for $\tilde{\Delta}$ over all subjects is 0.801, only lower than the value of $I2C2$ for GFA (0.871) and higher than $I2C2$ values for DTI-FA, ISO, and MD (0.798, 0.776, and 0.507 respectively; figure 3(A)). Using an exact test of differences [57] over 150 bootstrapped values of $I2C2$, calculated for each metric via resampling over subjects, we find that the $I2C2$ distribution for $\tilde{\Delta}$ is greater than the $I2C2$ distribution for DTI-FA, ISO, and MD with 55.3%, 87.3%, and 100% probability, respectively. The $I2C2$ distribution for $\tilde{\Delta}$ is less than the $I2C2$ distribution for GFA with 100% probability.

The distribution of ICC across all voxels in the common group mask has a median value of 0.790 for $\tilde{\Delta}$, which is similar to the value of $I2C2$ for $\tilde{\Delta}$ and indicates high reliability (figure 3(B)). For reference, we note that values of $ICC > 0.7$ imply high reliability in other imaging studies [54, 58, 59]. Using a two-sided Wilcoxon signed-rank test, we compare the ICC distribution for $\tilde{\Delta}$ with the ICC distributions for GFA (median 0.857), DTI-FA (median 0.796), ISO (median 0.735), and MD (median 0.454). In all cases $p < 0.001$ and the distribution medians are significantly different. Using a two-sided Kolmogorov–Smirnov test, we compare the shape of the ICC distribution for $\tilde{\Delta}$ to the shapes of the ICC distributions for GFA (KS-statistic $D = 0.257$), DTI-FA ($D = 0.041$), ISO ($D = 0.285$), and MD ($D = 0.633$). In all cases $p < 0.001$ and distribution shapes are significantly different.

Reproducibility. We find that our metric $\tilde{\Delta}$ is fairly reproducible according to its distribution of CV_{WS} across all voxels in the common group mask, with a median value of 0.142 (figure 3(C)). In other imaging studies, values of $CV_{WS} < 0.1$ imply high reproducibility [54, 58]. Using a two-sided Wilcoxon signed-rank test, we compare the CV_{WS} distribution for $\tilde{\Delta}$ with CV_{WS} distributions for GFA (median 0.077), DTI-FA (median 0.100), ISO (median 0.070), and MD (median 0.069). In all cases $p < 0.001$ and the distribution medians are significantly different. Using a two-sided Kolmogorov–Smirnov test, we compare the shape of the CV_{WS} distribution for $\tilde{\Delta}$ to the shapes of the CV_{WS} distributions for GFA (KS-statistic $D = 0.716$), DTI-FA ($D = 0.488$), ISO ($D = 0.923$), and MD ($D = 0.776$). In all cases $p < 0.001$ and distribution shapes are significantly different. Our results indicate that $\tilde{\Delta}$, although a reliable differentiator of individuals, is slightly less reproducible across scans than the other metrics investigated.

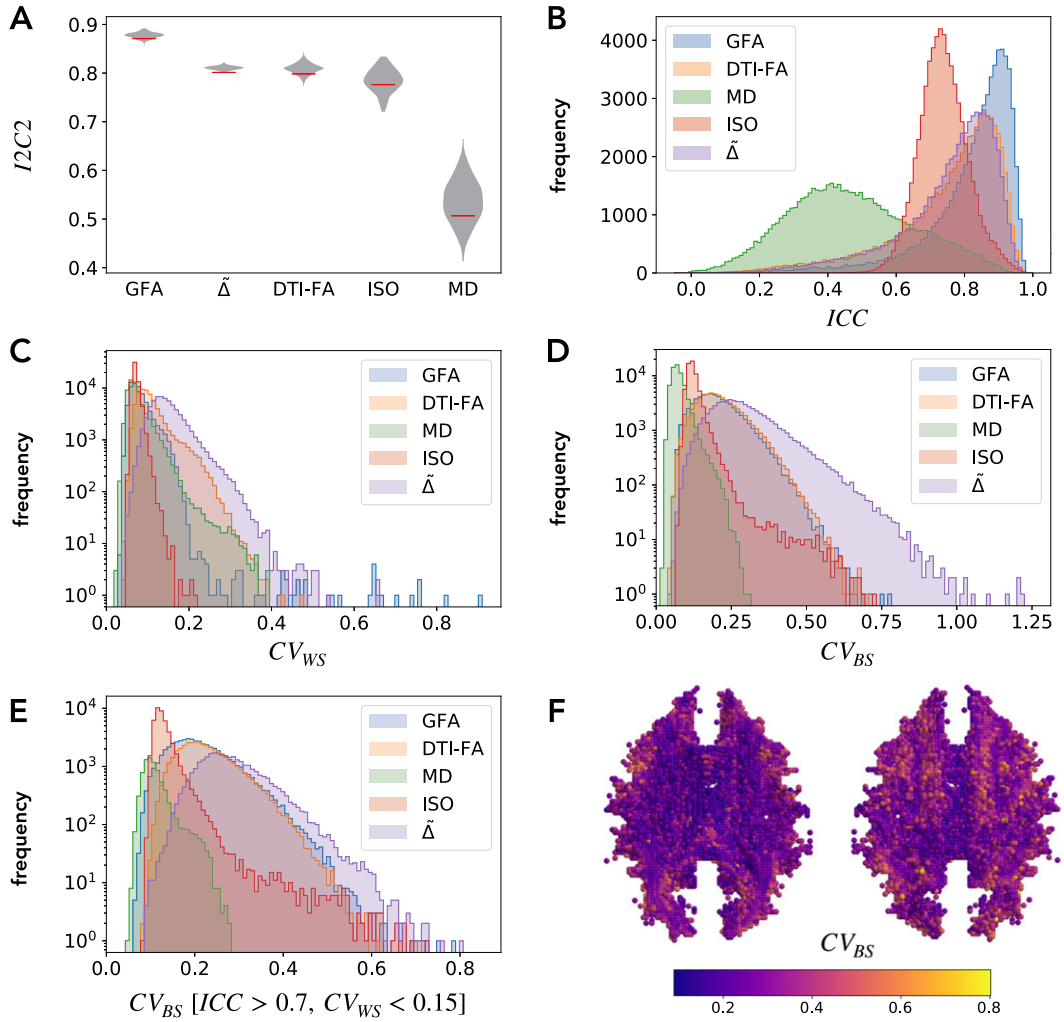

Figure 3. Crystallinity is reliable and reproducible across scans and has high inter-subject variability. (A) Image intra-class correlation coefficient (*I2C2*) calculated over the CRASH dataset for four common structural metrics as well as our metric ($\tilde{\Delta}$). Red bars denote *I2C2* measured over the full set of subjects, and violin plots show the distribution of *I2C2* values obtained via bootstrapping in which we resample subjects 150 times with replacement and calculate *I2C2* over each resample for all metrics. (B) Histograms of intra-class correlation coefficient $ICC(3,1)$ (denoted *ICC* in the panel) over all voxels of the CRASH dataset. (C) Histograms of the within-subject coefficient of variation, CV_{WS}, over all voxels of the identical dataset. (D) Histograms of the between-subject coefficient of variation, CV_{BS}, over all voxels of the identical dataset. (E) Histograms of CV_{BS} for only those voxels with reliable and reasonably reproducible values of each metric, determined by $ICC(3,1) > 0.7$ and $CV_{WS} < 0.15$. (F) Two views of a map of CV_{BS} for $\tilde{\Delta}$ for the voxels shown in panel (E). Voxels are colored by CV_{BS} according to the color bar below the images. The view on the left shows an axial slice of the image, and the view on the right is the flipside of the view on the left, showing the exterior of the image.

Individual variability. Crystallinity for a large subset of voxels in the common group mask is more variable across subjects than the other metrics analyzed, according to distributions of CV_{BS} for all metrics (figure 3(D)). The median value of CV_{BS} for $\tilde{\Delta}$ is 0.274, and that distribution has a prominent tail. Using a two-sided Wilcoxon signed-rank test, we again compare the CV_{BS} distribution for $\tilde{\Delta}$ with CV_{BS} distributions for GFA (median 0.193), DTI-FA (median 0.203), ISO (median 0.120), and MD (median 0.071). In all cases $p < 0.001$ and the distribution medians are significantly different. Using a two-sided Kolmogorov–Smirnov test, we compare the shape of the CV_{BS} distribution for $\tilde{\Delta}$ to the shapes of the CV_{BS} distributions for GFA (KS-statistic $D = 0.373$), DTI-FA ($D = 0.330$), ISO ($D = 0.853$), and MD ($D = 0.931$). In all cases $p < 0.001$ and the distribution shapes are significantly different.

Even within the more restrictive subset of voxels that are somewhat reproducible, with $CV_{WS} < 0.15$, and reliable, with $ICC(3,1) > 0.7$, the individual variability of $\tilde{\Delta}$ measured by CV_{BS} is high in comparison with the other diffusion metrics (figure 3(E)). For this voxel subset, the median of CV_{BS} for $\tilde{\Delta}$ is 0.273, still with a rather prominent tail. A two-sided Kolmogorov–Smirnov test shows that the shape of this distribution is significantly different than the shapes of the CV_{BS} distributions for GFA (median 0.204, KS-statistic $D = 0.407$), DTI-FA (median 0.219, KS-statistic $D = 0.335$), ISO (median 0.124, KS-statistic $D = 0.900$), and MD (median 0.104, KS-statistic $D = 0.909$). In all cases $p < 0.001$. The Wilcoxon

signed-rank test cannot be performed in this case, because the distributions have differing sizes. A map of CV_{BS} for $\tilde{\Delta}$ over these voxels (figure 3(F)) shows that voxels with reliable, fairly reproducible, and across-subject variable values of $\tilde{\Delta}$ tend to be located on the gray matter and lateral surfaces, rather than the white matter and medial surfaces. We speculate that the longer multi-voxel length scale over which $\tilde{\Delta}$ describes structure, in contrast to the shorter within-voxel length scale over which the other metrics describe structure, may contribute to the persistence of higher inter-subject variability of $\tilde{\Delta}$ with respect to the other metrics even for this restrictive set of voxels. Indeed, partitioning per-subject crystallinity values of this restrictive voxel set into two groups of high and low CV_{BS} reveals that the voxels with higher CV_{BS} are likely to have higher crystallinity (supplementary figure S5). This trend holds true across subjects, indicating perhaps that crystallinity captures structural information of especially high inter-subject variability. To test this hypothesis in the future, the reliability, reproducibility, and inter-subject variability of $\tilde{\Delta}$ should be compared to those same features for other metrics that also describe structure on a multi-voxel length scale.

3.3. Crystalline regions of the brain

We now turn to a more thorough investigation of crystallinity throughout the brain, again via analysis of the scans collected in the CRASH study. We examine the spatial distribution of crystallinity in two ways. First, we generate a voxel map of crystallinity, averaged over all analyzed subjects and all scans. Second, we segment each scan into neuroanatomical regions using a common white matter parcellation, and measure crystallinity throughout each region. In general, we find that crystalline voxels are located towards the center of the brain, in the corona radiata, internal capsule, corpus callosum, and uncinate fasciculus. Our findings are consistent with the results reported in section 3.1.

The subject-averaged spatial distribution of crystallinity throughout the brain, in the master template space discussed in section 3.2, is shown in figure 4(A). Each voxel is colored according to its value of $\langle\tilde{\Delta}\rangle_{\text{scan, subj}}$, the average value of $\tilde{\Delta}$ over all scans for all subjects. Figure 4(B) contains a thresholded version of the map in figure 4(A), showing only voxels with the lowest 10% of $\tilde{\Delta}$ values. The averaged crystallinity varies smoothly throughout the brain, and more crystalline regions of the brain are localized in white matter rather than in grey matter.

To gain more insight into the crystallinity of specific regions of the brain, we utilize a popular white matter parcellation, the JHU atlas described in the *Methods*, to group voxels into neuroanatomical regions. We then calculate distributions of $\tilde{\Delta}$ in each white matter region, pooled over all subjects and all scans. In contrast to the analysis presented previously, we warp the JHU white matter atlas into each subject's native space in this analysis, to avoid interpolating vector-valued images into a template space. To perform the warping, we use the *genericlabel* interpolation method in ANTs [36]. Figure 4(C) shows distributions of $\tilde{\Delta}$ in each white matter region according to the JHU atlas. Supplementary table S1 lists the average value and standard deviation of $\tilde{\Delta}$ within each white matter region.

We highlight regions of especially low $\tilde{\Delta}$ (high crystallinity) and high $\tilde{\Delta}$ (low crystallinity) with colored bars. We indicate the locations of these regions in a sample scan in figures 4(D) and (E). Highly crystalline regions include the internal capsule, splenium and genu of the corpus callosum, corona radiata, and uncinate fasciculus. These are white matter tracts near the center of the brain with various connective purposes [2, 26]. Interestingly, several of these tracts were found to be particularly vulnerable to schizophrenia, bipolar disorder, and autism spectrum disorder [27]. Regions of low crystallinity are located in the fornix, tapetum, and cerebellar peduncle.

3.4. Parcellation according to crystal grain

Finally, we explore the parcellation of white matter into 'crystal grains', or spatially contiguous communities of voxels that are structurally more similar to each other than expected on average (see *Methods*). We find that, despite its anatomy-blind automation, our crystal grain parcellation still results in white matter regions of anatomical interest. These crystal grains are a novel alternative to existing fiber bundling schemes such as BUndle ANalytics (BUAN) [60], because they do not divide the brain into known white matter fascicles, but instead into data-driven parcels of crystalline white matter. Our approach may thus prove useful in future white matter segmentation studies, perhaps when used in combination with fiber bundling methods.

We first show an example parcellation by crystal grain in figures 5(A) and (B) to demonstrate that crystal grains are anatomically meaningful by eye and contain useful structural information. We consider the same Stanford HARDI image as that analyzed in section 3.1, and color crystal grains of size 100 voxels or greater, detected using the community resolution parameter $\gamma = 1.1$ (figure 5(A)). Crystal grains are roughly symmetric across hemispheres and follow the anatomical branching of large white matter tracts. A closer look at grains deep within the brain near the corpus callosum (figure 5(B)) shows the hemispheric symmetry further, as well as the composite structural environments of individual grains.

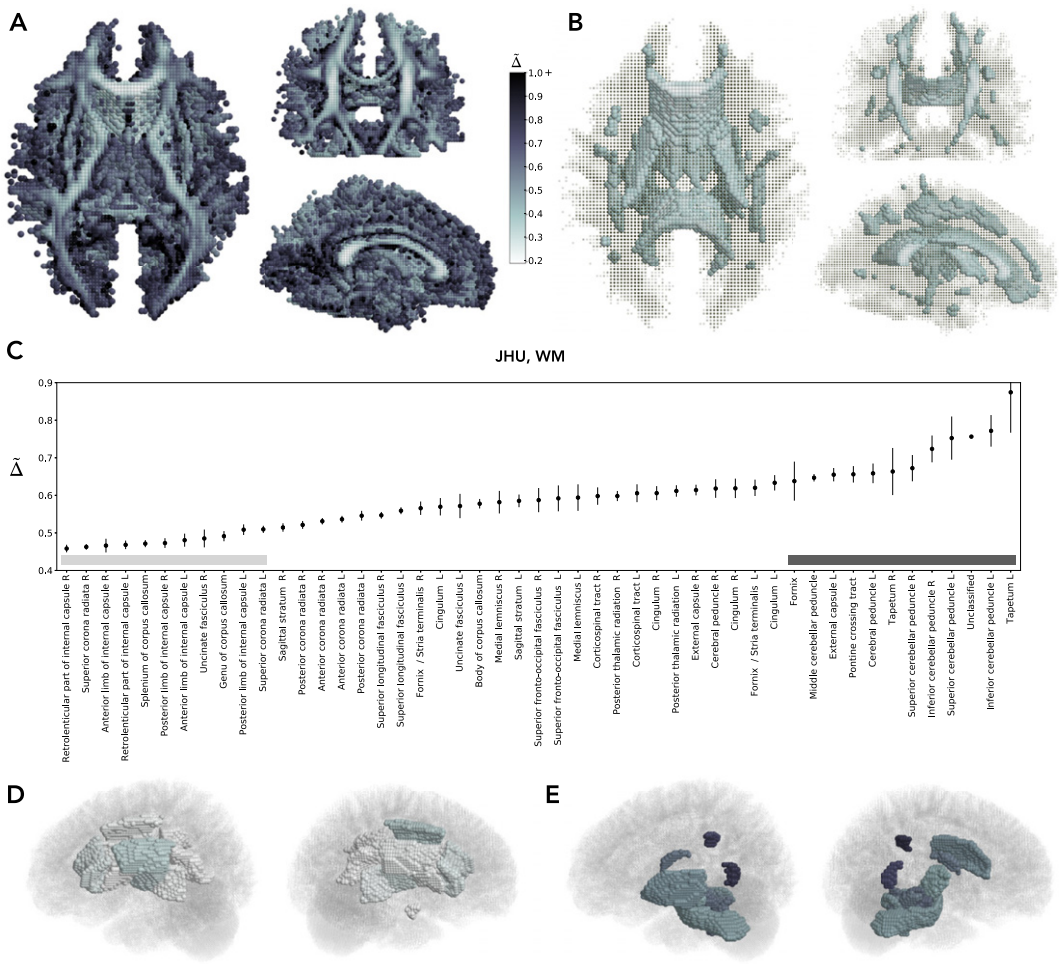

Figure 4. Identification of crystalline regions of white matter. (A) Three views of the crystallinity proxy $\tilde{\Delta}$ averaged over all analyzed subjects and all scans of the CRASH dataset, shown in a master template space as described in the main text. Each voxel is colored by average $\tilde{\Delta}$ according to the color bar to the right of the images. Voxels with lower values of $\tilde{\Delta}$ are lighter (more crystalline), and voxels with higher values of $\tilde{\Delta}$ are darker (less crystalline). (B) Thresholded views identical to those shown in panel (A), where only the (most crystalline) voxels with the lowest 10% of $\tilde{\Delta}$ values are shown. Voxels are also colored according to the color bar of panel (A). (C) Crystallinity proxy $\tilde{\Delta}$ of voxels in white matter regions according to the JHU white matter atlas (described in the main text), pooled over all subjects and all sessions. White matter regions are denoted with their formal anatomical names, and circles show the mean value of $\tilde{\Delta}$ in each region, taken across all subjects and all sessions. Error bars show the standard deviation of $\tilde{\Delta}$ within each region, normalized by the square root of the mean number of voxels in each region (taken across all subjects and all sessions). Regions are organized by increasing mean $\tilde{\Delta}$. ((D) and (E)) The most (D) and least (E) crystalline white matter regions in a sample scan, according to the pooled results over subjects and sessions shown in panel (C). The most crystalline regions are marked with a light gray bar in panel (C), and the least crystalline regions are marked with a dark gray bar. Each region is colored according to its average value of $\tilde{\Delta}$.

We next compute crystal grains in all scans of the CRASH dataset, and compare pooled results from our parcellation scheme to the commonly used JHU white matter atlas introduced in the *Methods*. We perform crystal grain segmentation over a weighted network for each subject, where weights are defined as in the *Methods* and averaged over all sessions of the subject. We vary the community resolution parameter γ for each subject, and find significant overlap between our crystal grain parcellation and the JHU atlas (warped into each subject's native space as detailed in the previous section) over a range of γ for all subjects (figure 5(C)). Partition overlap is measured via two distinct metrics, the adj. RAND index and adj. MI, both described in the *Methods*, to show that trends in overlap with γ are general and do not depend on the specific overlap measure. Both overlap measures peak between $\gamma = 1.0$ and $\gamma = 1.1$. Visual inspection of our crystal grain parcellation of the subject with highest adj. MI with the JHU atlas (at $\gamma = 1.05$) confirms that the segmentation is in fact similar to the JHU atlas (figure 5(D)). We find mesoscale crystal grains that resemble white matter regions in the JHU atlas, yet are completely determined by automatic detection of homogeneous brain tissue architecture. We further investigate similarities between this crystal grain parcellation and the JHU atlas by constructing a one-to-one mapping between each JHU atlas region and its optimally matched crystal grain. To construct this mapping, we build a confusion matrix C, where C_{ij} is the number of voxels that make up the intersection between JHU atlas region i and crystal grain j. We then

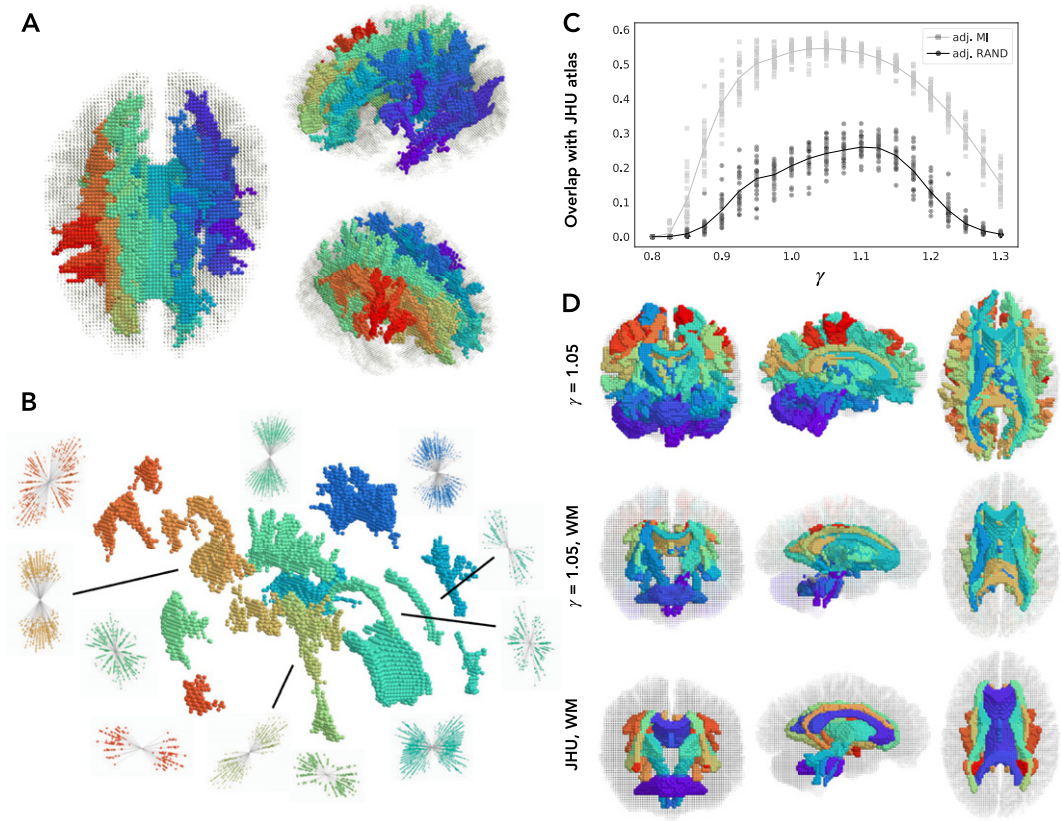

Figure 5. Parcellation of white matter into clusters of voxels with similar structure, or 'crystal grains'. (A) Three views of a sample diffusion image, colored according to crystal grain. Voxels are colored identically if they are members of the same crystal grain. Voxels colored black (and smaller in size for ease of visibility) are members of crystal grains of 100 or fewer voxels. (B) Select crystal grains shown in panel (A), with associated composite diffusion signals. Each composite signal is colored identically to its associated crystal grain, and connecting lines are drawn when the association is not clear. Composite diffusion signals are represented via ball-and-stick models for all peak vectors, and peak vectors for all voxels in each crystal grain are shown simultaneously. (C) Measures of partition similarity between our segmentation according to crystal grain and the common JHU white matter atlas, computed over scans in the CRASH dataset. adj. MI is shown in gray and adj. RAND score is shown in black as a function of community resolution parameter γ. Each marker is a measure of partition similarity for one subject, averaged over its sessions, and lines denote averages across subjects. Similarity is significant over a range of γ values, and peaks especially around $\gamma \sim 1.0$–1.1. (D) Three views of our crystal grain parcellation of the subject with highest adj. MI with the JHU atlas, at $\gamma = 1.05$. Voxels are colored identically if they are members of the same crystal grain of size >100 voxels. The top row of images shows the full crystal grain segmentation, while the middle row shows only those voxels in identified white matter regions according to the JHU atlas. The JHU atlas itself is shown in the bottom row of images for comparison; each white matter region in the atlas is colored an identical, random color. Similar anatomical structures can be seen in each white matter parcellation.

perform (cost-maximizing) linear sum assignment using the confusion matrix as the 'cost' matrix, to find the optimally matched crystal grain for each JHU atlas region such that the total number of overlapping voxels between all pairs is maximized [61, 62]. To perform this optimization, we use the linear sum assignment algorithm implemented in the Python package *scipy* [63]. Note that, since there are more crystal grains than JHU atlas regions, many crystal grains are not matched to any JHU atlas region using this method. Our matching results are tabulated in supplementary table S2 and detailed in supplementary figure S6, showcasing the similarities between the parcellations. In sum, our results underscore the potential for incorporating crystallinity into future white matter parcellation strategies.

3.5. Diffusion signal shape characterization

While crystallinity provides important information regarding the homogeneity of diffusion signals within a local region of voxels, characterization of the diffusion signal shape itself within each voxel is also of interest within the neuroimaging community. For this purpose, tools from soft matter may also be useful; we briefly explore one such structural characterization tool here. We use sets of orientational order parameters—usually denoted by Q_l in soft matter literature and used to describe symmetries of particle clusters [29]—to describe the shape of each diffusion signal in each voxel, and show that these Q_l shape descriptors provide an easily calculable, succinct means of determining whether the diffusion signal shape is especially unidirectional (representing a coherent white matter fiber bundle), bidirectional (representing a fiber crossing), or noisy. Each diffusion signal shape can be described with a shape descriptor consisting of

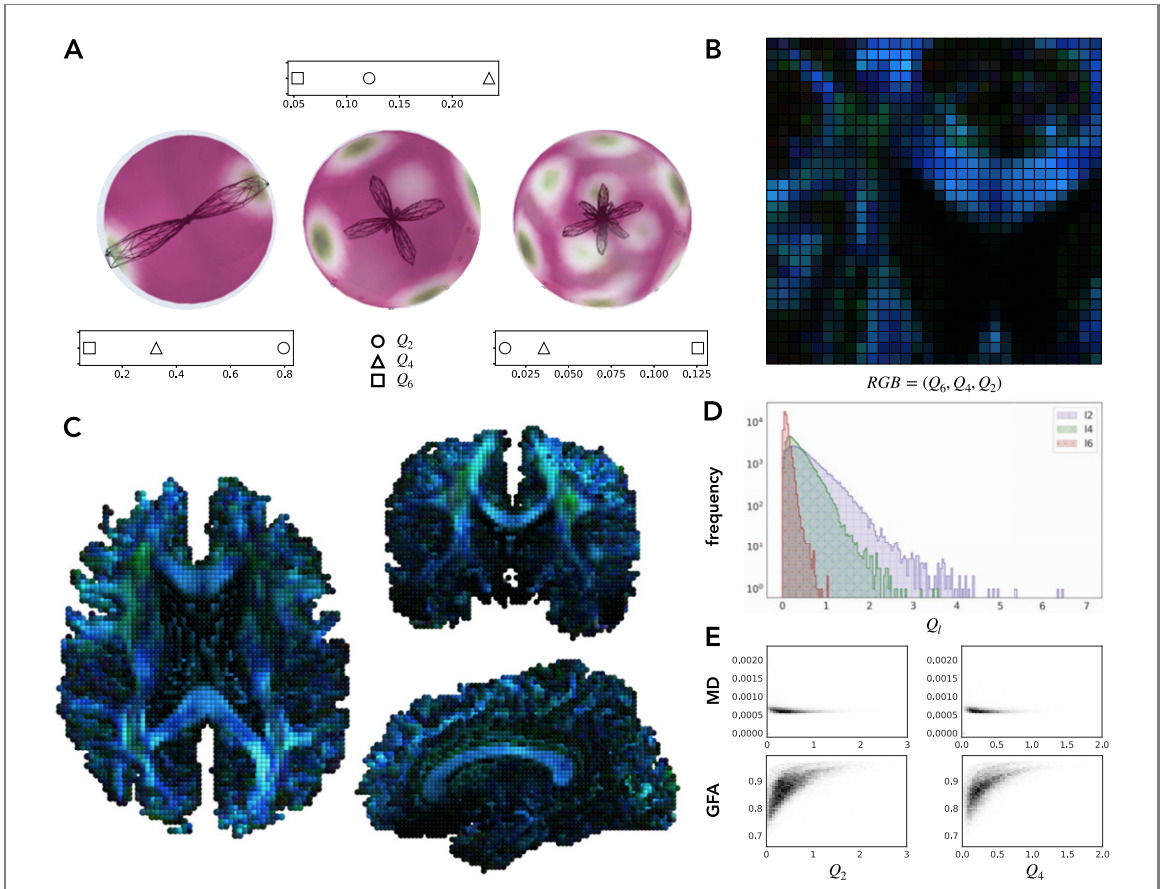

Figure 6. Orientational order parameters characterize diffusion signal shape. (A) Three fiber ODFs with different shapes are shown in black at the center of their corresponding probability density distributions on the unit sphere. Higher probability density is colored green, and lower probability density is colored pink. Above or below each ODF, corresponding values of orientational order parameters Q_2 (circles), Q_4 (triangles), and Q_6 (squares) are shown. (B) A slice of an example HARDI image, with voxels colored according to orientational order parameters Q_2, Q_4, and Q_6. For each voxel, (Q_6, Q_4, Q_2) is converted to an (R, G, B) color according to $\min(Q_l, 1)$. (C) Three views of a full sample image, with voxels colored according to orientational parameters $(Q_6, Q_4, Q_2) = (\text{R}, \text{G}, \text{B})$. Each Q_l parameter is converted to the appropriate color channel according to $\min(Q_l, 1.25)$. Voxels that appear cyan are those for whom $Q_2 > 1.25$ and $Q_4 > 1.25$, resulting in equal mixing of the blue and green channels. (D) Histograms of Q_l for all voxels of this sample scan for $l = 2$ (blue vertical cross-hatch), $l = 4$ (green diagonal cross-hatch), and $l = 6$ (red dots). (E) Joint histograms of Q_2 (left) and Q_4 (right) against MD (top) and GFA (bottom) accumulated over all voxels of this sample scan.

three orientational order parameters (Q_2, Q_4, Q_6); this description acts as a fingerprint (of only three dimensions) for the shape of the signal that is quite distinct from other diffusion metrics like MD and GFA. Calculation of the Q_l parameters is described in the *Methods*.

To show that the set (Q_2, Q_4, Q_6) differentiates between various diffusion signal shapes, we show three examples of fiber ODFs (unidirectional, crossing, and noisy), their corresponding probability density distributions on the unit sphere, and values of orientational order parameters Q_2, Q_4, and Q_6 for each of them (figure 6(A)). The especially unidirectional ODF's value of Q_2 is significantly higher than the other order parameters; the crossing ODF's value of Q_4 is significantly higher than the other order parameters; and the noisier ODF's value of Q_6 is highest, although absolute values for all parameters are different across ODFs. Viewing the parameters (Q_2, Q_4, Q_6) together thus communicates significant rotationally-invariant information regarding fascicles, crossings, and general noise.

We demonstrate the ability of the parameters (Q_2, Q_4, Q_6) to distinguish between fascicles, crossings, and noise in a real dataset by visualizing them in the example Stanford HARDI image discussed previously (figures 6(B)(C)). We visualize (Q_2, Q_4, Q_6) simultaneously as blue, green, and red channels respectively when coloring each voxel. Voxels with ODFs that are mostly uniaxial are mostly blue in color, as their values of Q_2 are highest. Voxels with ODFs that indicate fiber crossings and therefore are biaxial are more green, as they contain higher values of Q_4. Darker voxels contain noisier ODFs, as all values of Q_l are lower in magnitude. Although Q_6 is generally higher in these noisier voxels, they are not significantly red in color, because all Q_l values in these voxels are low. In both the diffusion imaging slice in figure 6(B) and the three views of the whole scan shown in figure 6(C) (each identical to the views shown in figures 1(A) and 2(A) respectively), the corpus callosum and corona radiata emerge as regions of a more blue or cyan color, indicating highly structured white matter fascicles, and more green regions of crossing fibers can also be

seen at the juncture between large white matter tracts, particularly in the transverse section. Cumulative distributions of each Q_l parameter over the entire scan show the wider range of Q_2 with respect to the other parameters, and the wider range of Q_4 with respect to Q_6 (figure 6(D)).

We also show that the orientational order parameters Q_l contain novel information concerning each diffusion ODF, by directly comparing values of Q_2 and Q_4 of each voxel against corresponding values of MD and GFA (figure 6(E)). We find that the orientational Q_l parameters are weakly correlated with MD (Pearson correlation coefficients $\rho = -0.14$ and $\rho = -0.15$ for Q_2 and Q_4, respectively), and are more correlated with GFA (Pearson correlation coefficients $\rho = 0.64$ and $\rho = 0.63$ for Q_2 and Q_4, respectively), with the general trend that voxels of lower GFA tend to have lower values of Q_2 or Q_4. As GFA increases, however, voxels have wider ranges of both Q_2 and Q_4, illustrating the decoupling of orientational diffusion shape information from anisotropy. In part, this decoupling at high values of GFA is attributable to the fact that the Q_l parameters are, by design, directly dependent on ODF signal strength, while GFA is not. We explore this key difference in normalization and its implications for the decoupling of these parameters at high GFA in supplementary figure S7.

4. Discussion

We have demonstrated that structural characterization techniques popular in soft matter physics are also useful in the context of neuroimaging. Crystallinity, or diffusion signal homogeneity, is a promising marker of white matter microstructure. It provides white matter information that is distinct from that provided by other traditional diffusion metrics; it is reliable, reproducible, and variable across individuals; and it varies meaningfully throughout the brain, with large white matter bundles possessing more structural homogeneity than smaller white matter bundles or grey matter. Segmentation of white matter into crystal grains, or especially structurally similar regions, constitutes a parcellation informed by underlying brain tissue architecture that overlaps significantly with a commonly used white matter atlas. Finally, orientational order parameters from soft matter provide low-dimensional descriptors of diffusion signal shape, and readily pinpoint regions of white matter structures and fiber crossings. The following sections provide context for our work within the separate disciplines of neuroimaging and soft matter, consider the limitations of our methods, and outline possible future directions and extensions.

4.1. Prior methods to assess white matter microstructure

A major obstacle for dMRI is its high dimensionality. Most popular neuroimaging methods reduce this dimensionality by representing white matter structure with scalar values for each voxel that can be used in voxel-wise group analyses with standard statistical tools. Measures like (G)FA and MD represent structure *within* voxels, but omit information about ODF directionality and dispersion. Additionally, these values are difficult to interpret in biological terms [64]. Alternatively, fixel-based analyses [65] compare scalar values on each ODF lobe, providing greater specificity than voxel-based approaches. Fixels, however, do not consider the orientation of fixels relative to one another or across voxels. The integrity of larger white matter structures that exist across voxels is typically assessed through inter-voxel measures of coherence such as the lattice index [23], tensor overlap [24], or local diffusion homogeneity [17]. The first two metrics rely on simplified tensor models for diffusion that are not necessarily faithful representations of white matter structures, while the latter metric, although model-free, requires substantial diffusion data for its computation. Tractography can also be used to characterize larger white matter structures; in this method, analysis tends to focus on region-to-region connectivity instead of local multi-voxel volumes of white matter [66, 67]. The approach developed in this paper is distinct from all of these techniques, as it incorporates magnitude and direction *across voxels* to characterize structure in a manner that is model-free, simple to compute, and intuitively grounded in materials physics.

4.2. Common tools for structural characterization in soft matter

The methods to assess white matter microstructure that we have presented in this paper, namely local crystallinity and orientational order parameterized by Q_l, are only two of the many techniques developed over the past several decades for structural characterization within soft matter physics [68, 69]. Some of these techniques may also translate well to the description of brain structure, and we briefly review them here. Relevant methods use local signatures ranging from Voronoi cells [70, 71], to bond angles [72] or the topology of local bonding environments [73–75], to the Fourier coefficients of local bonding environments [29, 76–78] to identify local structure in particulate systems. Recent advancements have also been made in using machine learning to identify structures robustly and automatically [77–79]. A final method of note is polyhedral template matching [80], which (like crystallinity) relies on root-mean-squared deviations between local environments in real space to determine structure. Although this method and many of those

just described were developed to identify specific structures through comparison to candidate templates, they may be straight-forwardly modified to simply describe rather than identify structure in the context of the human brain.

4.3. Prior efforts to develop white matter parcellations

Parcellation, or the division of the brain into meaningful regions, is a critical step in understanding and summarizing the anatomical and functional characteristics of brain tissue. A majority of efforts in this vein have focused on developing parcellations for grey matter [81]. Although less common, parcellations have also been developed for subcortical white matter, which have proven particularly useful for distinguishing neuroanatomical structures and providing regions of interest for cross-subject comparisons [82]. Efforts to segment white matter typically fall into one of two categories: they might be informed by cortical connectivity, or else consist of fiber tracking and bundling in white matter alone [83]. It has been demonstrated recently that the latter method of fiber clustering results in more consistent white matter segmentation across subjects [84]. Our partition of voxels into 'crystal grains' is particularly relevant for fiber clustering, and can be regarded as an additional tool (among others) to be leveraged for this purpose. Other methods developed for fiber clustering include segmentation according to geodesic distance between diffusion tensors [85], a tensor dissimilarity metric grounded in information theory [86], Euclidean difference between diffusion tensors [87], and the tensor scalar product [88]; level set modeling [89]; graph cut optimization [90]; spectral segmentation [91]; combined tensor clustering and probabilistic connectivity mapping [92]; fuzzy, non-parametric segmentation [93]; and even segmentation by projection into a higher-dimensional space [94]. Our classification of voxels into crystal grains provides a physically intuitive, simple, structure-driven metric that might be used in addition to or in concert with any of these more complicated methods for a more accurate segmentation of white matter. Relatedly, these methods might be useful for corroboration of our white matter parcellation scheme or vice versa.

4.4. Methodological considerations and limitations

Our method of crystallinity characterization is limited in several ways, and may be improved in the future. First, we only use the peaks of each ODF signal to characterize the local white matter environment. Although this focus has the advantage of reducing the dimensionality needed to describe each ODF signal, it obviously results in a loss of signal information. Future efforts to determine structural homogeneity could rely on other shape matching methods that incorporate more information about each signal shape. Additionally, we compared structural environments using a greedy method to minimize their root-mean-squared deviation. This method, while fast and straight-forward, is not guaranteed to find the globally minimal deviation between the environments. Finding the global minimum amounts to solving the well-known assignment problem [95], and in the future we could replace our greedy algorithm with any of the algorithmic solutions to the assignment problem to compare structural environments and determine crystallinity. Finally, we note that we have characterized the crystallinity of each voxel via a metric that is normalized with respect to the signal strength of that voxel. We included this normalization to treat noisy signals of low strength on equal footing with clear signals of high strength, but a better normalization scheme in the future could be developed to actively weight noisy signals such that they are explicitly classified as disordered.

We also note that there is a difference in how 'crystallinity' is interpreted in the contexts of diffusion MRI and soft matter. The word implies organization at an atomic or molecular scale in materials science, but in human MRI our crystallinity measurement reflects coherent structures spanning cubic millimeters of space. It is critical to note that accurately measuring the homogeneity of water diffusion on a smaller, within-voxel scale would require a recently-developed diffusion imaging sequence known as q-space trajectory imaging (QTI) [96]. It would be interesting in the future to extend our analysis to sub-voxel tissue structures captured via QTI [97], to probe 'crystallinity' on a length scale approaching that of microns. Currently, however, since our method only uses ODF peaks and not lobe widths, it can be used in conjunction with standard linear diffusion encoding sequences that have been available on most MRI scanners for many years. The method is also applicable to data collected with recent technological advances in image formation that prioritize improvements in image fidelity, acceleration of acquisition, and increase in the signal-to-noise ratio [98, 99].

4.5. Future directions

A study in the immediate future will use the orientational order parameters Q_l introduced in this work to characterize white matter fiber crossings and streamlines in real datasets such as the CRASH dataset, to ascertain the robustness and reliability of this characterization method, and to investigate differences in

these parameters across individuals. We will also explore using the rotational invariance of these parameters for the purposes of brain registration and image correction.

We also look forward to using local crystallinity to investigate individual differences in brain structure that may occur as a result of sex, genetics, or physiology. Future studies will explore how structural homogeneity changes in white matter during development and aging [100–103], or over training [104–107], and if it varies with gene expression in distributed regions throughout the brain [108]. Moreover, our approach may prove useful in understanding the structural alterations that accompany various neurological and psychiatric disorders [109, 110], as evident either *in vivo* or post mortem [111–113] and in either large or small population-based studies [114]. For each dimension of variance, we will target questions such as: do associated statistics involving overall crystallinity change, or are shifts localized to certain regions? Which regions become more or less crystalline? Does crystallinity correlate with any other biomarkers gleaned from pertinent datasets? Additional tools from the soft matter community may also be leveraged to characterize local white matter structure in more detail, including automated structure classification via machine learning. These investigations will contribute to the growing body of knowledge regarding how white matter structure influences brain function.

5. Conclusion

Materials physics provides advanced approaches for describing the characteristics of soft matter, but these tools have not yet been used to understand the complex structure of human brain tissue. This study provides an initial step in that interdisciplinary direction. We have analyzed white matter microstructure in the human brain by calculating crystallinity, or diffusion signal homogeneity, and orientational order parameters that describe the shape of each diffusion signal. We found that crystallinity provides information distinct from that provided by other common diffusion metrics, has high test-retest reliability, and varies meaningfully across the brain along interpretable lines of anatomical difference. Parcellations of white matter into crystal grains, or regions with high structural similarity, are automated, informed by brain architecture, and have significant overlap with a common white matter atlas. Additionally, sets of orientational order parameters provide fingerprints of reduced dimensionality for each diffusion signal that are capable of locating regions of white matter fiber crossings and streamlines. Our study underscores the utility of expanding communication between the fields of soft matter physics and neuroimaging in ongoing efforts to understand the material properties of human brain tissue and its relevance for cognitive function.

6. Citation diversity statement

Recent work in several fields of science has identified a bias in citation practices such that papers from women and other minorities are under-cited relative to other papers in the field [115–121]. Here we sought to proactively consider choosing references that reflect the diversity of our field in thought, form of contribution, gender, and other factors. We obtained the predicted gender of the first and last author of each reference by using databases that store the probability of a first name being carried by a woman or a man [115, 122]. By this measure (and excluding self-citations to the first and last authors of our current paper, and papers whose authors' first names could not be determined), our references contain 12.04% woman(first)/woman(last), 19.44% man/woman, 13.89% woman/man, and 54.63% man/man categorization. This method is limited in that (a) names, pronouns, and social media profiles used to construct the databases may not, in every case, be indicative of gender identity and (b) it cannot account for intersex, non-binary, or transgender people. We look forward to future work that could help us to better understand how to support equitable practices in science.

Acknowledgments

We thank L Parkes, A Kahn, M Bertolero, P Fotiadis, S Patankar, and C Lindbergh for helpful discussions. We also thank M Engel for the use of the visualization package inJaVis. EGT and DSB are supported by the National Science Foundation Materials Research Science and Engineering Center at University of Pennsylvania (NSF Grant DMR-1120901), and the Paul G Allen Family Foundation. This work was also supported by the National Institute of Mental Health (NIMH; Grant Nos. R01MH113550, R01MH112847, RF1MH116920, and R01MH120482). The authors declare that they have no competing interests. The views and conclusions contained in this document are solely those of the authors.

Data availability statement

The data that support the findings of this study are available upon reasonable request from the authors.

ORCID iDs

Erin G Teich https://orcid.org/0000-0001-7553-7054
Matthew Cieslak https://orcid.org/0000-0002-1931-4734
Barry Giesbrecht https://orcid.org/0000-0002-1976-1251
Danielle S Bassett https://orcid.org/0000-0002-6183-4493

References

[1] Strominger N L, Demarest R J and Laemle L B 2012 *Noback's Human Nervous System* 7th edn (Totowa, NJ: Humana Press)
[2] Schmahmann J D, Smith E E, Eichler F S and Filley C M 2008 *Ann. New York Acad. Sci.* **1142** 266
[3] Budday S, Nay R, de Rooij R, Steinmann P, Wyrobek T, Ovaert T C and Kuhl E 2015 *J. Mech. Behav. Biomed. Mater.* **46** 318
[4] Johansen-Berg H 2010 *Curr. Opin. Neurol.* **23** 351
[5] Filley C M and Fields R D 2016 *J. Neurophysiol.* **116** 2093
[6] Salat D H 2013 *Diffusion MRI* (*From Quantitative Measurement to in Vivo Neuroanatomy*) 2nd edn (Amsterdam: Elsevier) pp 257–81
[7] Counsell S J, Ball G, Pandit A and Edwards A D 2013 *Diffusion MRI* (*From Quantitative Measurement to in Vivo Neuroanatomy*) 2nd edn (Amsterdam: Elsevier) pp 283–300
[8] Bodini B and Ciccarelli O 2013 *Diffusion MRI* (*From Quantitative Measurement to in Vivo Neuroanatomy*) 2nd edn (Amsterdam: Elsevier) pp 241–55
[9] Bosnell R, Giorgio A and Johansen-Berg H 2008 *Dev. Neurorehabil.* **11** 174
[10] Johansen-Berg H, Scholz J and Stagg C J 2010 *Front. Syst. Neurosci.* **4** 146
[11] Le Bihan D and Johansen-Berg H 2012 *Neuroimage* **61** 324
[12] Johansen-Berg H and Rushworth M F S 2009 *Annu. Rev. Neurosci.* **32** 75
[13] Behrens T E J and Johansen-Berg H 2005 *Phil. Trans. R. Soc.* B **360** 903
[14] Hagmann P, Jonasson L, Maeder P, Thiran J-P, Wedeen V J and Meuli R 2006 *RadioGraphics* **26** S205
[15] Behrens T E, Sotiropoulos S N and Jbabdi S 2013 *Diffusion MRI* (*From Quantitative Measurement to in Vivo Neuroanatomy*) 2nd edn (Amsterdam: Elsevier) pp 429–51
[16] Pfefferbaum A, Sullivan E V, Hedehus M, Lim K O, Adalsteinsson E and Moseley M 2000 *Magn. Reson. Med.* **44** 259
[17] Gong G 2013 *PLoS One* **8** e66366
[18] Douaud G *et al* 2011 *NeuroImage* **55** 880
[19] Rose S E, Chen F, Chalk J B, Zelaya F O, Strugnell W E, Benson M, Semple J and Doddrell D M 2000 *J. Neurol. Neurosurg. Psychiatry* **69** 528
[20] Fox R J, McColl R W, Lee J-C, Frohman T, Sakaie K and Frohman E 2008 *Arch. Neurol.* **65** 1179
[21] Du X-Q, Zou T-X, Huang N-X, Zou Z-Y, Xue Y-J and Chen H-J 2019 *J. Neurol. Sci.* **405** 116438
[22] Pierpaoli C, Barnett A, Pajevic S, Chen R, Penix L, Virta A and Basser P 2001 *NeuroImage* **13** 1174
[23] Pierpaoli C and Basser P J 1996 *Magn. Reson. Med.* **36** 893
[24] Basser P J and Pajevic S 2000 *Magn. Reson. Med.* **44** 41
[25] Hallgrímsson H T, Cieslak M, Foschini L, Grafton S T and Singh A K 2018 *NeuroImage* **172** 390
[26] Wycoco V, Shroff M, Sudhakar S and Lee W 2013 *Neuroimaging Clin.* **23** 197
[27] Koshiyama D *et al* 2020 *Mol. Psychiatr.* **25** 883
[28] Ennis D B and Kindlmann G 2006 *Magn. Reson. Med.* **55** 136
[29] Steinhardt P J, Nelson D R and Ronchetti M 1983 *Phys. Rev.* B **28** 784
[30] Garyfallidis E, Brett M, Amirbekian B, Rokem A, van der Walt S, Descoteaux M and Nimmo-Smith I 2014 *Front. Neuroinf.* **8** 1
[31] Tournier J-D, Calamante F and Connelly A 2007 *NeuroImage* **35** 1459
[32] Thurman S M *et al* 2018 *PLoS One* **13** e0191883
[33] Cieslak M *et al* 2021 QSIPrep: an integrative platform for preprocessing and reconstructing diffusion MRI data *Nat. Methods* **18** 775–8
[34] Veraart J, Novikov D S, Christiaens D, Ades-Aron B, Sijbers J and Fieremans E 2016 *Neuroimage* **142** 394
[35] Yeh F C, Wedeen V J and Tseng W-Y I 2010 *IEEE Trans. Med. Imag.* **29** 1626
[36] Avants B, Epstein C, Grossman M and Gee J 2008 *Med. Imag. Anal.* **12** 26
[37] Ramasubramani V, Dice B D, Harper E S, Spellings M P, Anderson J A and Glotzer S C 2020 *Comput. Phys. Commun.* **254** 107275
[38] Jeub L G S, Bazzi M, Jutla I S and Mucha P J 2011–2019 A generalized Louvain method for community detection implemented in MATLAB https://github.com/GenLouvain/GenLouvain
[39] Fortunato S 2010 *Phys. Rep.* **486** 75
[40] Newman M E J and Girvan M 2004 *Phys. Rev.* E **69** 026113
[41] Bassett D S, Owens E T, Porter M A, Manning M L and Daniels K E 2015 *Soft Matter* **11** 2731
[42] Papadopoulos L, Puckett J G, Daniels K E and Bassett D S 2016 *Phys. Rev.* E **94** 032908
[43] Good B H, de Montjoye Y-A and Clauset A 2010 *Phys. Rev.* E **81** 046106
[44] Mori S *et al* 2008 *NeuroImage* **40** 570
[45] Hubert L and Arabie P 1985 *J. Classif.* **2** 193
[46] Vinh N X, Epps J and Bailey J 2010 Information theoretic measures for clusterings comparison: Variants, properties, normalization and correction for chance *J. Mach. Learn. Res.* **11** 2837–54
[47] Pedregosa F *et al* 2011 Scikit-learn: Machine Learning in Python *J. Mach. Learn. Res.* **12** 2825–30

[48] Tuch D S 2004 *Magn. Reson. Med.* **52** 1358
[49] Jones D K 2013 *Diffusion MRI* (*From Quantitative Measurement to in Vivo Neuroanatomy*) 2nd edn (Amsterdam: Elsevier) pp 87–104
[50] Shrout P E and Fleiss J L 1979 *Psychol. Bull.* **86** 420
[51] McGraw K O and Wong S P 1996 *Psychol. Bull.* **1** 30
[52] Shou H, Eloyan A, Lee S, Zipunnikov V, Crainiceanu A N, Nebel M B, Caffo B, Lindquist M A and Crainiceanu C M 2013 *Cogn. Affect. Behav. Neurosci.* **13** 714
[53] Heiervang E, Behrens T E J, Mackay C E, Robson M D and Johansen-Berg H 2006 *NeuroImage* **33** 867
[54] Luque Laguna P A, Combes A J, Streffer J, Einstein S, Timmers M, Williams S C R and Dell'Acqua F 2020 *NeuroImage: Clinical* **26** 102168
[55] Bassett D S, Brown J A, Deshpande V, Carlson J M and Grafton S T 2011 *NeuroImage* **54** 1262
[56] Pfefferbaum A, Adalsteinsson E and Sullivan E V 2003 *J. Magn. Reson. Imag.* **18** 427
[57] MacKinnon J 2009 *Handbook of Computational Econometrics* ed D A Belsley and E Kontoghiorghes (New York: Wiley) pp 183–213
[58] Marenco S, Rawlings R, Rohde G K, Barnett A S, Honea R A, Pierpaoli C and Weinberger D R 2006 *Psychiatr. Res. Neuroimaging* **147** 69
[59] Somandepalli K *et al* 2015 *Dev. Cogn. Neurosci.* **15** 83
[60] Chandio B Q, Risacher S L, Pestilli F, Bullock D, Yeh F-C, Koudoro S, Rokem A, Harezlak J and Garyfallidis E 2020 *Sci. Rep.* **10** 17149
[61] Meilă M and Heckerman D 2001 *Mach. Learn.* **42** 9
[62] Hart C E, Sharenbroich L, Bornstein B J, Trout D, King B, Mjolsness E and Wold B J 2005 *Nucleic Acids Res.* **33** 2580
[63] Virtanen P *et al* 2020 *Nat. Methods* **17** 261
[64] Jones D K, Knösche T R and Turner R 2013 *NeuroImage* **73** 239
[65] Raffelt D A, Tournier J-D, Smith R E, Vaughan D N, Jackson G, Ridgway G R and Connelly A 2017 *NeuroImage* **144** 58
[66] Jbabdi S and Johansen-Berg H 2011 *Brain Connect.* **1** 169
[67] Ciccarelli O, Catani M, Johansen-Berg H, Clark C and Thompson A 2008 *Lancet Neurol.* **7** 715
[68] Keys A S, Iacovella C R and Glotzer S C 2011 *J. Comput. Phys.* **230** 6438
[69] Stukowski A 2012 *Modell. Simul. Mater. Sci. Eng.* **20** 045021
[70] Finney J L 1970 *Proc. R. Soc.* A **319** 479
[71] Tanemura M, Hiwatari Y, Matsuda H, Ogawa T, Ogita N and Ueda A 1977 *Prog. Theor. Phys.* **58** 1079
[72] Ackland G J and Jones A P 2006 *Phys. Rev.* B **73** 054104
[73] Honeycutt J D and Andersen H C 1987 *J. Phys. Chem.* **91** 4950
[74] Malins A, Williams S R, Eggers J and Royall C P 2013 *J. Chem. Phys.* **139** 234506
[75] Lazar E A, Han J and Srolovitz D J 2015 *Proc. Natl Acad. Sci.* **112** E5769
[76] Auer S and Frenkel D 2004 *J. Chem. Phys.* **120** 3015
[77] Phillips C L and Voth G A 2013 *Soft Matter* **9** 8552
[78] Spellings M and Glotzer S C 2018 *AIChE J.* **64** 2198
[79] Reinhart W F, Long A W, Howard M P, Ferguson A L and Panagiotopoulos A Z 2017 *Soft Matter* **13** 4733
[80] Larsen P M, Schmidt S and Schiøtz J 2016 *Modell. Simul. Mater. Sci. Eng.* **24** 055007
[81] Glasser M F *et al* 2016 *Nature* **536** 171
[82] Smith S M, Kindlmann G and Jbabdi S 2013 *Diffusion MRI* (*From Quantitative Measurement to in Vivo Neuroanatomy*) 2nd edn (Amsterdam: Elsevier) pp 209–39
[83] O'Donnell L J, Golby A J and Westin C-F 2013 *NeuroImage* **80** 283
[84] Zhang F, Norton I, Cai W, Song Y, Wells W M and O'Donnell L J 2017 *Proc. Int. Symp. Biomedical Imaging* p 796
[85] Lenglet C, Rousson M and Deriche R 2006 *2006 3rd IEEE Int. Symp. Biomedical Imaging: Macro to Nano* vol 1 (IEEE) pp 794–7
[86] Wang Z and Vemuri B C 2005 *IEEE Trans. Med. Imag.* **24** 1267
[87] Wang Z and Vemuri B C 2004 *Lecture Notes in Computer Science (Including Subseries Lecture Notes in Artificial Intelligence and Lecture Notes in Bioinformatics)* vol 3024 pp 304–15
[88] Jonasson L, Bresson X, Hagmann P, Cuisenaire O, Meuli R and Thiran J-P 2005 *Med. Imag. Anal.* **9** 223
[89] Zhukov L 2003 *J. Electron. Imag.* **12** 125
[90] Weldeselassie Y T and Hamarneh G 2007 DT-MRI segmentation using graph cuts *Medical Imaging 2007: Image Processing* (San Diego, United States of America, 2007) ed J P W Pluim and J M Reinhardt p 65121K
[91] Ziyan U, Tuch D and Westin C-F 2006 *Lecture Notes in Computer Science (Including Subseries Lecture Notes in Artificial Intelligence and Lecture Notes in Bioinformatics)* vol 4191 LNCS pp 807–14
[92] Barbieri S, Bauer M H A, Klein J, Moltz J, Nimsky C and Hahn H K 2012 *NeuroImage* **60** 1025
[93] Awate S P and Gee J C 2007 *Lecture Notes in Computer Science (Including Subseries Lecture Notes in Artificial Intelligence and Lecture Notes in Bioinformatics)* vol 4584 LNCS pp 296–307
[94] Jonasson L, Bresson X, Thiran J-P, Wedeen V J and Hagmann P 2007 *IEEE Trans. Med. Imag.* **26** 1547
[95] Aardal K, Nemhauser G L and Weismantel R (ed) 2005 *Discrete Optimization* (*Handbooks in Operations Research and Management Science*) vol 12 (Amsterdam: Elsevier)
[96] Westin C-F *et al* 2016 *NeuroImage* **135** 345
[97] Magdoom K N, Pajevic S, Dario G and Basser P J 2021 *Sci. Rep.* **11** 2766
[98] Wu W and Miller K L 2017 *J. Magn. Reson. Imag.* **46** 646
[99] Wu W, Koopmans P J, Andersson J L R and Miller K L 2019 *Magn. Reson. Med.* **82** 107
[100] Sexton C E, Walhovd K B, Storsve A B, Tamnes C K, Westlye L T, Johansen-Berg H and Fjell A M 2014 *J. Neurosci.* **34** 15425
[101] Krogsrud S K *et al* 2016 *NeuroImage* **124** 473
[102] Giorgio A, Santelli L, Tomassini V, Bosnell R, Smith S, De Stefano N and Johansen-Berg H 2010 *NeuroImage* **51** 943
[103] Giorgio A, Watkins K E, Douaud G, James A C, James S, De Stefano N, Matthews P M, Smith S M and Johansen-Berg H 2008 *NeuroImage* **39** 52
[104] Scholz J, Klein M C, Behrens T E J and Johansen-Berg H 2009 *Nat. Neurosci.* **12** 1370
[105] Sampaio-Baptista C *et al* 2013 *J. Neurosci.* **33** 19499
[106] Sexton C E *et al* 2020 *Physiol. Behav.* **223** 112923

[107] Tomassini V, Jbabdi S, Kincses Z T, Bosnell R, Douaud G, Pozzilli C, Matthews P M and Johansen-Berg H 2011 *Hum. Brain Mapp.* **32** 494
[108] Sampaio-Baptista C *et al* 2020 *Prog. Neurobiol.* **187** 101770
[109] McKavanagh R *et al* 2019 *Hum. Brain Mapp.* **40** 4417
[110] Kolind S, Matthews L, Johansen-Berg H, Leite M I, Williams S C R, Deoni S and Palace J 2012 *NeuroImage* **60** 263
[111] Miller K L *et al* 2011 *NeuroImage* **57** 167
[112] Roebroeck A, Miller K L and Aggarwal M 2019 *NMR Biomed.* **32** e3941
[113] Miller K L, McNab J A, Jbabdi S and Douaud G 2012 *NeuroImage* **59** 2284
[114] Miller K L *et al* 2016 *Nat. Neurosci.* **19** 1523
[115] Dworkin J D, Linn K A, Teich E G, Zurn P, Shinohara R T and Bassett D S 2020 *Nat. Neurosci.* **23** 918–26
[116] Maliniak D, Powers R and Walter B F 2013 *Int. Org.* **67** 889
[117] Caplar N, Tacchella S and Birrer S 2017 *Nat. Astron.* **1** 0141
[118] Chakravartty P, Kuo R, Grubbs V and McIlwain C 2018 *J. Commun.* **68** 254
[119] Thiem Y, Sealey K F, Ferrer A E, Trott A M and Kennison R 2018 *Just Ideas? The Status and Future of Publication Ethics in Philosophy: A White Paper* https://publication-ethics.org/
[120] Dion M L, Sumner J L and Mitchell S M 2018 *Polit. Anal.* **26** 312
[121] Bertolero M A *et al* 2020 Racial and ethnic imbalance in neuroscience reference lists and intersections with gender *bioRxiv Preprint* https://doi.org/10.1101/2020.10.12.336230 (accessed 21 November 2020)
[122] Zhou D, Cornblath E J, Stiso J, Teich E G, Dworkin J D, Blevins A S and Bassett D S 2020 Gender diversity statement and code notebook (v1.0) *Zenodo* https://doi.org/10.5281/zenodo.3672110